Chinese Chemical Letters 36 (2025) 110200

Contents lists available at ScienceDirect

Chinese Chemical Letters

journal homepage: www.elsevier.com/locate/cclet

# Solar-light-driven photocatalytic degradation and detoxification of ciprofloxacin using sodium niobate nanocubes decorated g-$C_3N_4$ with built-in electric field

Hui Wang[a], Haodong Ji[b,c,*], Dandan Zhang[c,d], Xudong Yang[c], Hanchun Chen[b], Chunqian Jiang[e,*], Weiliang Sun[c], Jun Duan[c], Wen Liu[c,f,g,*]

[a] Key Laboratory of Tree Breeding and Cultivation of National Forestry and Grassland Administration, Research Institute of Forestry, Chinese Academy of Forestry, Beijing 100091, China
[b] Eco-environment and Resource Efficiency Research Laboratory, School of Environment and Energy, Peking University Shenzhen Graduate School, Shenzhen 518055, China
[c] The Key Laboratory of Water and Sediment Sciences, Ministry of Education; College of Environmental Sciences and Engineering, Peking University, Beijing 100871, China
[d] Department of Energy, Environmental, and Chemical Engineering, Washington University, St. Louis, MO 63130, United States
[e] Research Institute of Forestry, Chinese Academy of Forestry, Beijing 100091, China
[f] School of Environmental Engineering, Wuhan Textile University, Engineering Research Centre for Clean Production of Textile Dyeing and Printing, Ministry of Education, Wuhan 430073, China
[g] Beijing National Laboratory for Molecular Sciences, Peking University, Beijing 100871, China

ARTICLE INFO

*Article history:*
Received 12 March 2024
Revised 14 June 2024
Accepted 1 July 2024
Available online 1 July 2024

*Keywords:*
Detoxification
Photocatalysis
Solar light
Ciprofloxacin
Reactive sites

ABSTRACT

Simultaneous degradation and detoxification during pharmaceutical and personal care product removal are important for water treatment. In this study, sodium niobate nanocubes decorated with graphitic carbon nitride (NbNC/g-$C_3N_4$) were fabricated to achieve the efficient photocatalytic degradation and detoxification of ciprofloxacin (CIP) under simulated solar light. $NaNbO_3$ nanocubes were *in-situ* transformed from $Na_2Nb_2O_6{\cdot}H_2O$ *via* thermal dehydration at the interface of g-$C_3N_4$. The optimized NbNC/g-$C_3N_4$–1 was a type-I heterojunction, which showed a high conduction band (CB) level of −1.68 eV, leading to the efficient transfer of photogenerated electrons to $O_2$ to produce primary reactive species, $^{\cdot}O_2^-$. Density functional theory (DFT) calculations of the density of states indicated that C 2p and Nb 3d contributed to the CB, and 0.37 $e^-$ transferred from $NaNbO_3$ to g-$C_3N_4$ in NbNC/g-$C_3N_4$ based on the Mulliken population analysis of the built-in electric field intensity. NbNC/g-$C_3N_4$–1 had 3.3- and 2.3-fold of CIP degradation rate constants ($k_1 = 0.173$ $min^{-1}$) compared with those of pristine g-$C_3N_4$ and $NaNbO_3$, respectively. In addition, N24, N19, and C5 in CIP with a high Fukui index were reactive sites for electrophilic attack by $^{\cdot}O_2^-$, resulting in the defluorination and ring-opening of the piperazine moiety of the dominant degradation pathways. Intermediate/product identification, integrated with computational toxicity evaluation, further indicated a substantial detoxification effect during CIP degradation in the photocatalysis system.



Broad-spectrum antibiotics, particularly second-generation fluoroquinolones, have been monitored worldwide in natural water matrices because of their high demand and extensive application in the treatment of diseases caused by bacterial infections [1]. Ciprofloxacin (CIP) is a typical fluoroquinolone antibiotic, which is frequently detected in the effluents of pharmaceutical manufacturing. The trace-level CIP with high ecotoxicity will severely threaten human health and the safety of the natural ecosystem [2]. Therefore, efficient treatment strategies and technologies are urgently required.

Considering the deficiencies in the biodegradability and mineralization rate of antibiotics, conventional treatment processes using activated sludge cannot efficiently remove CIP, and transformation products (TPs) may have higher ecotoxicity [3-6]. Photocatalysis is a cost-efficient and environmentally friendly technology that has gained increasing attention for the treatment of antibiotics such as CIP [7]. Compared to other technologies, photocatalysis has specific advantages such as solar light utilization, moderate reac-

* Corresponding authors.
*E-mail addresses:* jihaodong@pku.edu.cn (H. Ji), jiangchq@caf.ac.cn (C. Jiang), wen.liu@pku.edu.cn (W. Liu).

https://doi.org/10.1016/j.cclet.2024.110200
1001-8417/

tion conditions and low secondary pollution [8]. More importantly, photocatalysis can effectively mineralize various antibiotics to non-toxic final products such as $H_2O$ and $CO_2$ [9]. Recently, metal-free graphitic carbon nitride (g-$C_3N_4$), synthesized *via* a facile thermal polymerization method, has been proposed as a promising photocatalyst owing to its medium band gap (~2.65 eV), high photogenerated carrier transfer efficiency, and good stability. Thus, g-$C_3N_4$ has been widely applied for photocatalytic degradation of various organic contaminants [10,11]. However, the practical application of g-$C_3N_4$ is limited by its deficiencies in light absorption and conversion in the visible light range, electron transfer efficiency and recoverability [12]. More importantly, the photoinduced electron-hole pairs generally possess a higher recombination ratio in g-$C_3N_4$, leading to a low utilization rate of photogenerated carriers [11,12].

Various strategies have been developed to improve the photocatalytic activity of neat g-$C_3N_4$, In particular, heterostructure/heterojunction construction has been widely proven as an adequate approach for enhancing its photocatalytic activity [13]. Compared with other heterojunctions (type-II, Z-scheme and S-scheme), the type-I heterojunction facilitates the efficient separation of electron-hole pairs and controls the hole transfer direction and accumulation, resulting in the construction of a stable photocatalyst and the formation of a built-in electric field [14]. However, few studies reported type-I heterojunctions because of the special band energy levels of the two semiconductors. Thus, it is necessary to precisely regulate type-I heterojunctions coupled with g-$C_3N_4$.

Sodium niobate ($NaNbO_3$), which has thermoelectric, piezoelectric, and ferroelectric properties [15,16], is a potential candidate for environmental photocatalysis applications. In addition, $NaNbO_3$ with a high valence band level exhibits strong oxidation ability owing to the generation of rich reactive species, such as photoinduced holes ($h^+$) and hydroxyl radicals ($^{\bullet}OH$), which are suitable for micropollutant degradation. In addition, incorporation of $NaNbO_3$, as a new electron donor level, can increase the electrons density and transfer efficiency, thus the introduction of $NaNbO_3$ with high photocatalytic ability in composite material is a potential method for improving photocatalytic performance [17]. Therefore, modification of g-$C_3N_4$ with $NaNbO_3$ to construct type-I heterojunctions will boost electron transfer, assuming the positive effect of "$1+1>2$" during the organic pollutant elimination process. In addition, the morphology and structure of $NaNbO_3$ could be controlled by varying the synthesis conditions. Therefore, the *in-situ* coordinated 3-D cubic $NaNbO_3$ from $Na_2Nb_2O_6{\cdot}H_2O$ shows better photocatalytic activities because of the crystal plane heterogeneity, thus facilitating photoexcited electron transfer in the type-I heterojunction of g-$C_3N_4$ [18,19].

In this study, an $NaNbO_3$ nanocube-decorated g-$C_3N_4$ nanohybrid (NbNC/g-$C_3N_4$) was synthesized and used for the photocatalytic degradation of CIP under simulated solar light. Energy-band structures were designed to achieve efficient electron transfer. The photocatalytic detoxification efficiency of CIP was evaluated. The mechanism of reactive species production was revealed through material characterization and radical identification. In addition, the reaction mechanism of CIP attack by radicals was investigated *via* integrated experimental analysis and computational calculations.

All chemicals and reagents used in the experiments were of analytical grade or higher without further purification, as provided in Text S1(Supporting information). NbNC/g-$C_3N_4$ was synthesized *via* a two-step route, *i.e.*, $Na_2Nb_2O_6{\cdot}H_2O$ (precursor of $NaNbO_3$) and g-$C_3N_4$ were prepared first, followed by a calcination process to achieve *in-situ* transformation and decoration of $NaNbO_3$ onto g-$C_3N_4$. Detailed synthesis methods are shown in Text S2 (Supporting information). The synthesized materials were characterized by field-emission scanning electron microscopy (SEM), high-resolution transmission electron microscopy (HRTEM), X-ray diffraction (XRD), X-ray photoelectron spectroscopy (XPS), Fourier transform infrared spectroscopy. In addition, UV–vis spectrophotometry, photocurrent, electrochemical impedance spectroscopy (EIS), photoluminescence spectra (PL), linear sweep voltammetry (LSV) and Brunauer-Emmett-Teller (BET) nitrogen adsorption were also analyzed to obtain the diffuse reflectance spectra (DRS), photoelectrochemical properties, surface area, and pore properties of the catalysts. The detailed material characterization methods are described in Text S3 (Supporting information).

Batch experiments on the photocatalytic performance were performed in a quartz reactor (volume = 250 mL) with a water-cooling system to maintain the reaction temperature at 25 °C (Fig. S1 in Supporting information). A Microsolar 300 solar-light simulator (Beijing Perfectlight, Beijing, China) coupled with a Xe lamp (300 W) was used and operated at a light irradiation of 100 ± 0.5 mW/cm$^2$ in the AM 1.5 G mode. The typical photocatalytic test was conducted with 10 μmol/L CIP (100 mL) and 0.1 g/L catalysts in the reactor, and the pH was adjusted to 7.0 ± 0.1 by NaOH or $HClO_4$ (0.1 mol/L). The CIP concentration was detected using a Dionex UltiMate 3000 high-performance liquid chromatograph (HPLC, Thermo Fisher Scientific). The TPs and degradation intermediates were determined using an ultra-HPLC equipped with an electrospray ionization source and a triple quadrupole mass spectrometer (Dionex UltiMate 3000 Series; MS, Thermo Scientific, USA) [20]. The detailed analytical methods are described in Text S4 (Supporting information).

Density functional theory (DFT) calculations on CIP are performed using Gaussian 16 software (Version C.01) [21]. B3LYP combined with 6–31+G(d,p) is applied for structure optimization [22,23]. Details of the calculation method for the Fukui index are described in Text S5 (Supporting information). To investigate the theoretical ecotoxicity of CIP and its TPs [3]. The Cambridge Sequential Total Energy Package in Materials Studio 2020 was used to calculate the band gap, density of state (DOS), projected DOS (PDOS), work function, electron density, and electron density difference (EDD) of the materials (Text S6 in Supporting information) [24-26]. g-$C_3N_4$ exhibits a smooth surface and 2-D layered structure (Figs. 1a-g), while pristine $Na_2Nb_2O_6{\cdot}H_2O$ exhibited as 1-D nanorods (Figs. 1b and e), and the lattice distance of 0.15 nm

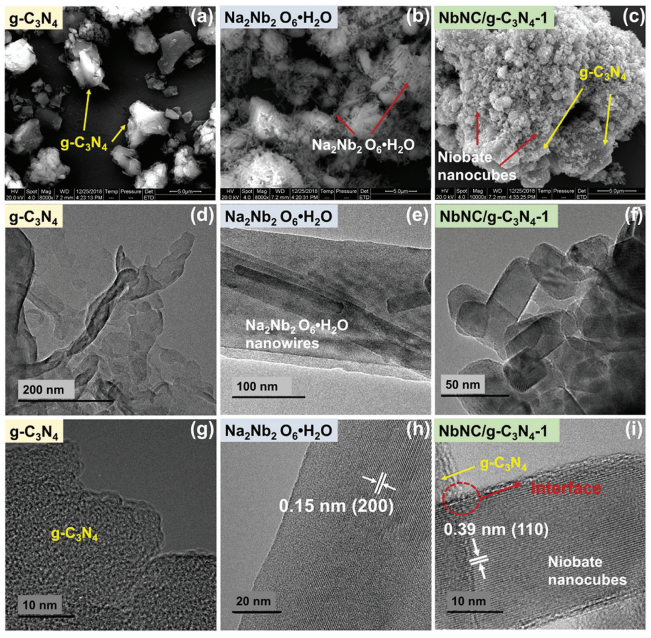


**Fig. 1.** (a-c) Field emission scanning electron microscopy (FESEM), (d-f) TEM and (g-i) HRTEM images of g-$C_3N_4$, $Na_2Nb_2O_6{\cdot}H_2O$ and NbNC/g-$C_3N_4$–1.

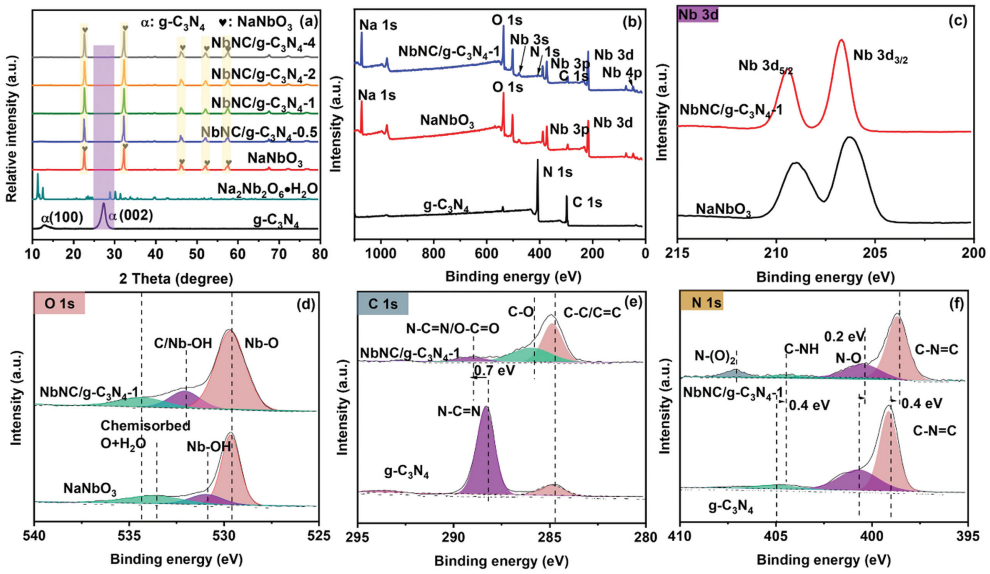


**Fig. 2.** (a) XRD patterns of NbNC/g-$C_3N_4$ with different component ratios. The XPS spectra of $NaNbO_3$, g-$C_3N_4$ and NbNC/g-$C_3N_4$–1: (b) The survey, (c) Nb 2p, (d) O 1s, (e) C 1s and (f) N 1s.

displayed in the HRTEM image was indexed to the (200) plane of $Na_2Nb_2O_6{\cdot}H_2O$ (Fig. 1h) [27,28]. After calcination treatment for the *in-situ* formation and decoration of $NaNbO_3$ onto g-$C_3N_4$, the $Na_2Nb_2O_6{\cdot}H_2O$ 1-D nanowires were transformed to $NaNbO_3$ 3-D nanocubes *via* dehydration (Fig. 1f) due to the more thermodynamically stability than $NaNbO_3$ nanowires [27]. In addition, the surface of NbNC/g-$C_3N_4$–1 was coarse owing to the niobate decoration (Fig. 1c). The measured lattice distance of 0.39 nm in NbNC/g-$C_3N_4$–1 was assigned to the (110) plane of orthorhombic $NaNbO_3$ (JCPDS 01–073–0803) (Fig. 1i), indicating the different crystalline structures for pristine $Na_2Nb_2O_6{\cdot}H_2O$ and $NaNbO_3$ phase in NbNC/g-$C_3N_4$–1. The successful hybridization of the $NaNbO_3$ nanocubes and g-$C_3N_4$ can enhance the utilization of solar light, thus facilitating electron transfer to achieve better photocatalytic effectiveness for CIP degradation. In addition, an interface connection between g-$C_3N_4$ and $Na_2Nb_2O_6$ phases is clearly observed in Fig. 1i, allowing the electrons transfer between these two components and beneficial to the built-in electric field construction [29].

In the XRD patterns (Fig. 2a), the significant peaks of pristine g-$C_3N_4$ at 13.0° and 27.5° were assigned to the (100) and (002) crystalline planes (JCPDS 01–087–1526), respectively, which can be characterized as the tri-*s*-triazine system in the interlayer structure and stacking of aromatic units [30]. For pristine $Na_2Nb_2O_6{\cdot}H_2O$, the $2\theta$ peaks at 11.4°, 12.7°, 29.1°, 30.4°, and 31.6° corresponded to monoclinic crystal $Na_2Nb_2O_6$ with a *C2/c* space group ($a = 17.114$ Å, $b = 5.0527$ Å, and $c = 16.5587$ Å), comprising [$NbO_6$] octahedra lattice [31]. For pristine $NaNbO_3$ formed after thermal dehydration from $Na_2Nb_2O_6{\cdot}H_2O$, new distinct peaks at 22.8°, 32.5°, 46.5°, 52.4°, and 57.9° appeared, assigned to the (110), (114), (220), (118), and (028) planes of the orthorhombic crystal structure (JCPDS 01–073–0803) (Fig. S2 in Supporting information), respectively, with the *Pbcm* space group ($a = 5.506$ Å, $b = 5.566$ Å, and $c = 15.520$ Å). An "octahedral tilting" [$NbO_6$] octahedra corner-sharing network was displayed, indicating that structure fabrication along with phase transformation occurred during dehydration of $Na_2Nb_2O_6{\cdot}H_2O$, *i.e.*, the [$NbO_6$] layers and chemical bonding (Nb–O–Nb and Nb–O–Na) were atomically rearranged to [$NbO_6$] octahedra *via* the thermal excitation due to the minimization of Gibbs free energy, resulting in the formation of $NaNbO_3$ nanocubes (Figs. 1e and f). For all NbNC/g-$C_3N_4$ nanohybrids, all the $Na_2Nb_2O_6{\cdot}H_2O$ peaks disappeared while the diffractions of $NaNbO_3$ emerged, indicating the *in-situ* crystalline phase transformation *via* calcination.

Figs. 2b-f show the XPS spectra of materials. In the high-resolution Nb 3d spectrum (Fig. 2c), the two significant split peaks at 206.1 eV and 208.9 eV for pristine $NaNbO_3$ are assigned to the Nb $3d_{3/2}$ and $3d_{5/2}$ orbitals, respectively. The spin-orbit separation energy of 2.8 eV corresponded to the [$NbO_6$] octahedra [32]. There was a positive shift (+0.5 eV) for the two Nb orbitals for NbNC/g-$C_3N_4$–1 (Table S1 in Supporting information), indicating electron transfer from $NaNbO_3$ to g-$C_3N_4$ and the formation of chemical bonds for Nb. In the high-resolution spectra of O 1s (Fig. 2d), the peaks at 529.6, 530.9, and 533.6 eV for pristine $NaNbO_3$ indexed to the lattice O derived from the [$NbO_6$] octahedra, Nb–OH, and chemisorbed $O/H_2O$, respectively. For NbNC/g-$C_3N_4$–1, the atomic percentage of lattice O increased from 63.07 at% ($NaNbO_3$) to 70.39 at% (NbNC/g-$C_3N_4$–1) (Table S1), indicating the formation of Nb–O–C or Nb–O–N, except the main chemical bond Nb–O–Nb in the [$NbO_6$] octahedra [33]. In the high-resolution spectra of C 1s (Fig. 2e), the peaks at 284.8 eV and 288.3 eV in pristine g-$C_3N_4$ corresponded to C–C/C=C and N–C=N of the triazine rings, respectively [4]. The N–C=N peak decreased dramatically from 85.16 at% for g-$C_3N_4$ to 9.82 at% for NbNC/g-$C_3N_4$–1 (Table S1), indicating new bond formation for C. Moreover, a new peak at *ca.* 285.9 eV assigned to C–O (accounting for 38.33 at% of C) increased in NbNC/g-$C_3N_4$–1, which was in good agreement with the formation of Nb–O–C.

Fig. S3a (Supporting information) shows the photocatalytic effectiveness of various photocatalysts for CIP degradation. The adsorption of CIP was first assessed for all materials (Figs. S3a and S4 in Supporting information). Neat g-$C_3N_4$ barely adsorbed CIP in 30 min, while neat $NaNbO_3$ displayed a CIP adsorption efficiency of 39.0%. In addition, the NbNC/g-$C_3N_4$ composites showed CIP adsorption efficiencies of 10.0%-16.9%, indicating efficient interaction between CIP and NbNC/g-$C_3N_4$ materials. Then, a *pseudo*-first order model was used to interpret the kinetic results (Table S2 in Supporting information) [34,35]. 64.1% and 84.5% of CIP was degraded by pristine g-$C_3N_4$ and $NaNbO_3$ with degradation kinetic rate constants ($k_1$) of 0.052 and 0.076 $min^{-1}$, respectively. Enhanced photocatalytic effectiveness of CIP degradation was observed using all NbNC/g-$C_3N_4$ nanohybrids. Specifically, NbNC/g-$C_3N_4$–1 ($Na_2Nb_2O_6{\cdot}H_2O$: g-$C_3N_4$ mass ratio of 1:1) exhibited the

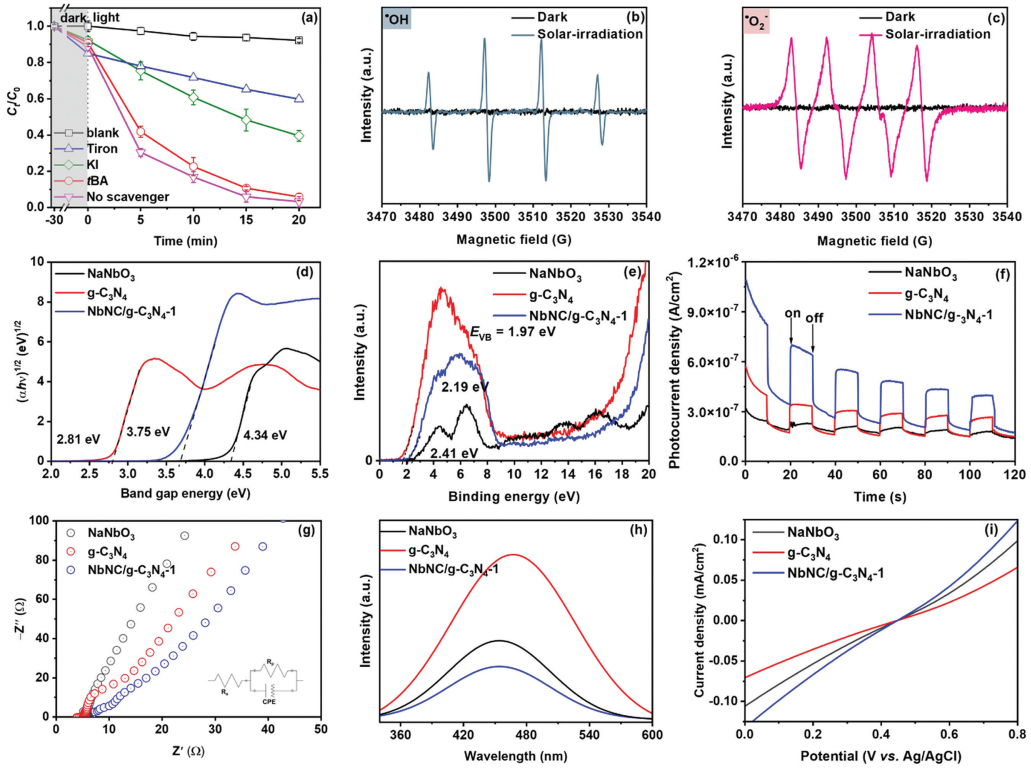


**Fig. 3.** (a) Photocatalytic degradation of CIP by NbNC/g-$C_3N_4$–1 in the presence of various scavengers (Initial CIP concentration = 10 μmol/L, catalyst dosage = 0.1 g/L, temperature = 25 ± 0.2 °C, solution pH = 7.0 ± 0.1, scavenger dosage = 10 mmol/L). ESR spectra of (b) DMPO-•OH and (c) DMPO-•$O_2^-$. (d) $E_g$ values calculated from Kubelka-Munk method. (e) XPS-VB spectra and (f) photocurrent spectra for pristine $NaNbO_3$, g-$C_3N_4$, and NbNC/g-$C_3N_4$–1. (g-i) EIS, PL and LSV curves of pristine $NaNbO_3$, g-$C_3N_4$ and NbNC/g-$C_3N_4$–1.

highest $k_1$ value (0.173 $min^{-1}$), which was 3.3 and 2.3 times that of pristine g-$C_3N_4$ and $NaNbO_3$, respectively. Fig. S3b (Supporting information) shows that the optimum NbNC/g-$C_3N_4$–1 dosage was 0.10 g/L, with a high CIP removal efficiency of 96.8%; further increasing the dosage to 0.20 g/L achieved a slight increase in the CIP removal efficiency to 99.3%.

After scavenger quenching tests, Fig. 3a shows that the addition of Tiron and potassium iodide (KI) inhibited CIP degradation by 56.5% and 36.3% at 20 min, respectively, indicating that •$O_2^-$ played the most important role, whereas $h^+$ contributed less (Table S3 in Supporting information). However, the addition of *tert*-butyl alcohol (*t*BA) slightly retarded the photocatalytic degradation of CIP by 2.6%, suggesting that •OH plays a negligible role. The electron spin resonance (ESR) spectra further confirmed the generation of •OH and •$O_2^-$ in the NbNC/g-$C_3N_4$–1 photocatalytic system under solar irradiation (Figs. 3b and c).

Based on the UV–vis DRS spectra (Fig. S5 in Supporting information), the measured $E_g$ for $NaNbO_3$, g-$C_3N_4$, and NbNC/g-$C_3N_4$–1 were 4.34, 2.81, and 3.75 eV, respectively (Fig. 3d). The synthesized $NaNbO_3$ in this study had a markedly wider band gap energy; therefore, the highest occupied molecular orbital (HOMO) and lowest unoccupied molecular orbital (LUMO) were introduced to describe its energy levels instead of the valance band (VB) and conduction band (CB). The light absorption edge of NbNC/g-$C_3N_4$–1 was red-shifted, with a narrower band gap (3.75 eV) than that of pristine $NaNbO_3$ (286 nm, 4.34 eV), indicating the enhanced light utilization efficiency of the new material. Although g-$C_3N_4$ exhibited an absorption edge in the visible light region at 441 nm and an $E_g$ of 2.81 eV, NbNC/g-$C_3N_4$–1 showed higher photocatalytic activity owing to efficient charge migration and electron-hole separation. In addition, the calculated $E_{VB}$ and $E_{CB}$ were 2.07 and −1.68 eV for NbNC/g-$C_3N_4$–1, respectively (Fig. 3e), and negative $E_{CB}$ values led to higher electron reactivity on CB, facilitating the production of •$O_2^-$. The photocurrent spectra clearly show that the photoelectric conversion efficiency of NbNC/g-$C_3N_4$–1 was better than that of pristine $NaNbO_3$ and g-$C_3N_4$ (Fig. 3f). Besides, EIS spectra in Fig. 3g display that NbNC/g-$C_3N_4$–1 with a smaller arc radius possessed a lower resistance for charge transfer and higher charge transfer efficiency than pristine g-$C_3N_4$ and $NaNbO_3$. Then, PL spectra in Fig. 3h also present that NbNC/g-$C_3N_4$–1 with a lower steady-state PL emission intensity than g-$C_3N_4$ and $NaNbO_3$, suggesting NbNC/g-$C_3N_4$–1 had a lower recombination rate of photoinduced electron-hole pairs than the other two materials. Finally, LSV curves in Fig. 3i show that NbNC/g-$C_3N_4$–1 had a stronger current density and redox capacity than pristine g-$C_3N_4$ and $NaNbO_3$, indicating the electrical conductivity and photocatalytic performance has been obviously enhanced after the heterojunction construction [36].

To explore the mechanism on enhanced photocatalytic activity of NbNC/g-$C_3N_4$, the band structure, DOS/PDOS spectra, electron density, work function, and EDD were studied *via* DFT calculations (Fig. 4). The structural models of the catalysts are presented in Figs. S6a and b (Supporting information). The calculated band gap of pure g-$C_3N_4$ (Fig. 4a) and $NaNbO_3$ (Fig. S6c in Supporting information) were 1.281 and 2.373 eV, respectively. The obtained band gap values are lower than the experimental values because of the known limitations of the plain DFT method [36]. Fig. 4d shows that NbNC/g-$C_3N_4$ possesses a more negative CB than pure g-$C_3N_4$, indicating that the CB of NbNC/g-$C_3N_4$ has a high electronic reactivity. In the PDOS spectra for NbNC/g-$C_3N_4$ (Fig. 4e), the N 2p and O 2p orbitals primarily contributed to the VB, whereas the C 2p and Nb 3d orbitals contributed to the CB. Hence, the electron transfer path in NbNC/g-$C_3N_4$ followed: N 2p → O 2p → Nb 3d → C 2p based on the PDOS distributions. Meanwhile, Fig. 4e shows that

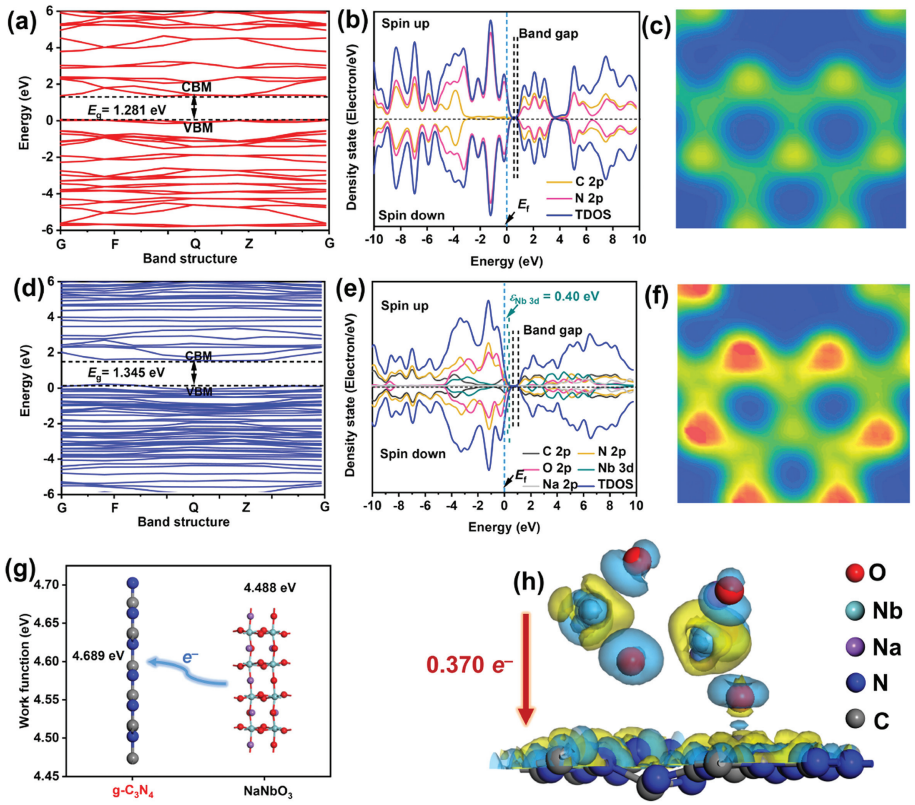


**Fig. 4.** (a) The band structure, (b) DOS spectra and (c) electron density of pure g-$C_3N_4$. (d) The band structure, (e) DOS spectra and (f) electron density of NbNC(110)/g-$C_3N_4$. (g) The work function of g-$C_3N_4$ and $NaNbO_3$. (h) EDD of NbNC(110)/g-$C_3N_4$ (yellow region: electrons depletion; cyan region: electrons accumulation).

the PDOS of N 2p moves to the left for NbNC/g-$C_3N_4$ compared to that of pure g-$C_3N_4$, indicating that the electron density of N 2p increased after the introduction of $NaNbO_3$ and more electrons were transferred along the above path under light irradiation. Moreover, the d-band center of Nb 3d in NbNC/g-$C_3N_4$ shifts to 0.40 eV compared with 0.44 eV of $NaNbO_3$ (Fig. 4e and Fig. S6d in Supporting information), which can be attributed to the compositing with g-$C_3N_4$. Based on the PDOS of Nb 3d in Fig. 4e, an antibonding state is formed at nearly 2 eV compared to pure $NaNbO_3$ (Fig. S6d), suggesting that $d_{x^2-y^2}$ orbitals with higher coupling ability combine with p orbitals during the bond formation of Nb–O–N/Nb–O–C. Accordingly, the introduction of g-$C_3N_4$ changes the electronic structure of Nb 3d orbitals, further leading to the alteration of d band center [37]. Therefore, the d-band center of NbNC/g-$C_3N_4$ was markedly closer to the Fermi level, suggesting that the electrons in Nb 3d were more reactive and could be more effectively transferred to C 2p with higher catalytic activity [38]. The electron density images (Figs. 4c and f) show higher electron densities in the N 2p and C 2p spectra of NbNC/g-$C_3N_4$ than those of g-$C_3N_4$, which benefits the photocatalytic reaction. The work function (Fig. 4g) indicates that $NaNbO_3$ with a low value (4.488 eV) transfers electrons to g-$C_3N_4$ with a high value (4.689 eV) when the NbNC/g-$C_3N_4$ heterojunction is constructed. EDD analysis indicates that electrons are more likely to transfer from $NaNbO_3$ to g-$C_3N_4$ (Fig. 4h); thus, holes accumulated on $NaNbO_3$ and electrons gathers on g-$C_3N_4$ [38,39]. The EDD result clearly shows a 0.37 $e^-$ transfer from $NaNbO_3$ to g-$C_3N_4$ based on the Mulliken population analysis of the built-in electric field intensity. Furthermore, because the $e^-$ transfer direction is from $NaNbO_3$ to g-$C_3N_4$ based on the EDD result in $NaNbO_3$/g-$C_3N_4$ composite, the $e^-$ density is greatly increased in g-$C_3N_4$, and the built-in electric field is also constructed because of their electrons density difference. Thus, g-$C_3N_4$ can be likened to a switch with a large amount of $e^-$, and more $e^-$ transfer occurs along N 2p → O 2p → Nb 3d → C 2p chain under light irradiation, leading to a high $e^-$ utilization rate and activity [40]. Thus, the electron density increased in g-$C_3N_4$ and the formed built-in electric field significantly boost the separation rate of charge carriers, further promoting photocatalytic activity [39].

Fig. S7 (Supporting information) shows a schematic of efficient charge migration at the interface of NbNC/g-$C_3N_4$–1 nanohybrid during photocatalysis. Based on the energy levels of $NaNbO_3$ and g-$C_3N_4$, the NbNC/g-$C_3N_4$–1 structure is a type-I heterojunction. Then, under light irradiation, the photogenerated electrons and holes transfer to the same side [14,41]. Specifically, the LUMO potential of $NaNbO_3$ (−1.93 V) is more negative than the CB of g-$C_3N_4$ (−0.84 V; Fig. S7), which helps the movement of photogenerated electrons from the LUMO of $NaNbO_3$ to the CB of g-$C_3N_4$. In addition, the photogenerated holes cannot move from the VB of g-$C_3N_4$ (+1.97 V) to the HOMO of $NaNbO_3$ (+2.41 V) because of the greater negativity of the VB of g-$C_3N_4$. The transformation of these photogenerated electrons by heterojunctions and the generation of holes in the HOMO and VB can reduce the charge recombination rate and provide more electrons/holes on the surface of the photocatalyst [14,41]. The photocurrent intensity in Fig. 3f and the DFT calculations in Fig. 4 prove the efficient separation of electron-hole pairs compared with neat g-$C_3N_4$ and $NaNbO_3$; thus, an internal electric field can also be generated during electron transfer from $NaNbO_3$ to g-$C_3N_4$.

To accurately evaluate the reactive sites of the CIP molecule, DFT calculations of CIP were conducted based on the natural population analysis charge distribution (Fig. 5). Fig. 5b shows the HOMO is placed on the piperazine ring, and the C atom of the benzene ring is bonded with the F atom, which are the most reactive sites for electron loss [42]. Furthermore, the piperazine ring side of $CIP^{\pm}$ with a high positive ESP at neutral pH preferred to attach on the negative-charged surface of NbNC/g-$C_3N_4$–1 (Fig. 5c). Fig. 5d indi-

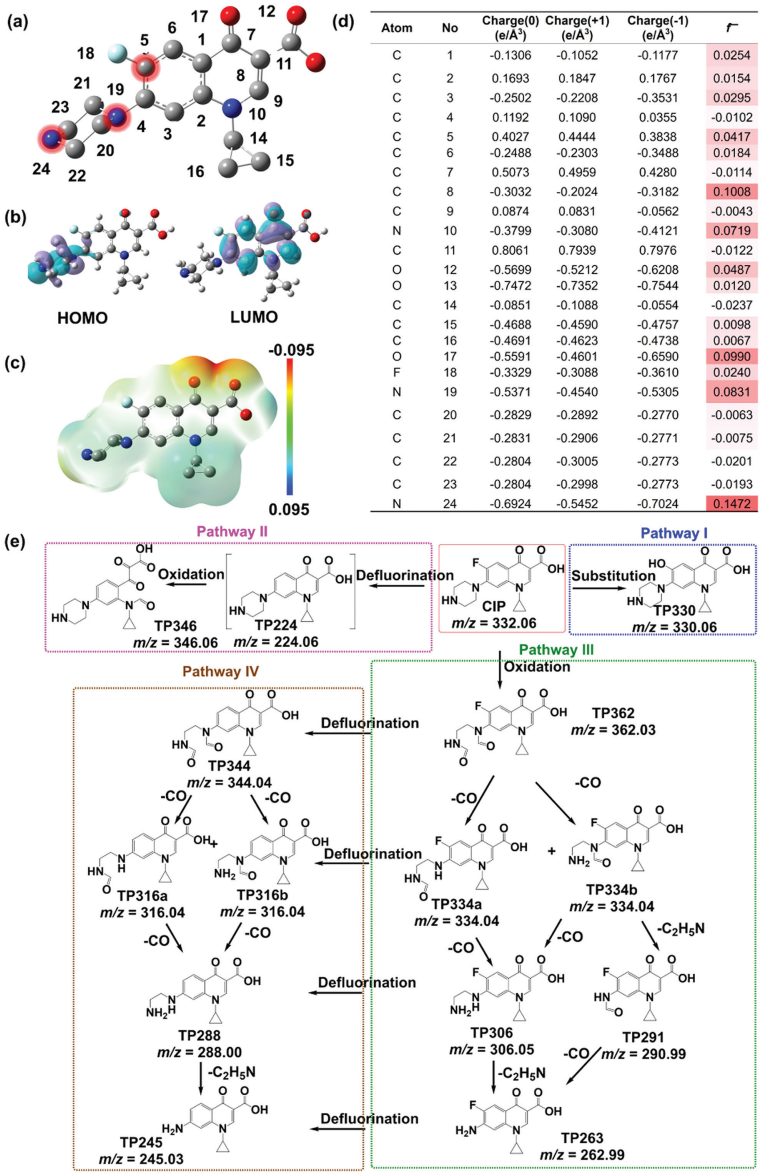


| Atom | No | Charge(0) (e/Å³) | Charge(+1) (e/Å³) | Charge(-1) (e/Å³) | f⁻ |
|---|---|---|---|---|---|
| C | 1 | -0.1306 | -0.1052 | -0.1177 | 0.0254 |
| C | 2 | 0.1693 | 0.1847 | 0.1767 | 0.0154 |
| C | 3 | -0.2502 | -0.2208 | -0.3531 | 0.0295 |
| C | 4 | 0.1192 | 0.1090 | 0.0355 | -0.0102 |
| C | 5 | 0.4027 | 0.4444 | 0.3838 | 0.0417 |
| C | 6 | -0.2488 | -0.2303 | -0.3488 | 0.0184 |
| C | 7 | 0.5073 | 0.4959 | 0.4280 | -0.0114 |
| C | 8 | -0.3032 | -0.2024 | -0.3182 | 0.1008 |
| C | 9 | 0.0874 | 0.0831 | -0.0562 | -0.0043 |
| N | 10 | -0.3799 | -0.3080 | -0.4121 | 0.0719 |
| C | 11 | 0.8061 | 0.7939 | 0.7976 | -0.0122 |
| O | 12 | -0.5699 | -0.5212 | -0.6208 | 0.0487 |
| O | 13 | -0.7472 | -0.7352 | -0.7544 | 0.0120 |
| C | 14 | -0.0851 | -0.1088 | -0.0554 | -0.0237 |
| C | 15 | -0.4688 | -0.4590 | -0.4757 | 0.0098 |
| C | 16 | -0.4691 | -0.4623 | -0.4738 | 0.0067 |
| O | 17 | -0.5591 | -0.4601 | -0.6590 | 0.0990 |
| F | 18 | -0.3329 | -0.3088 | -0.3610 | 0.0240 |
| N | 19 | -0.5371 | -0.4540 | -0.5305 | 0.0831 |
| C | 20 | -0.2829 | -0.2892 | -0.2770 | -0.0063 |
| C | 21 | -0.2831 | -0.2906 | -0.2771 | -0.0075 |
| C | 22 | -0.2804 | -0.3005 | -0.2773 | -0.0201 |
| C | 23 | -0.2804 | -0.2998 | -0.2773 | -0.0193 |
| N | 24 | -0.6924 | -0.5452 | -0.7024 | 0.1472 |

**Fig. 5.** (a) CIP$^{\pm}$ chemical structure. (b) HOMO and LUMO of CIP$^{\pm}$. (c) ESP of CIP$^{\pm}$. (d) NPA charge distribution and Fukui index ($f^-$) of CIP$^{\pm}$. (e) Proposed pathways on photocatalytic degradation of CIP by NbNC/g-$C_3N_4$–1 under solar light. (Initial CIP concentration = 10 μmol/L, catalyst dosage = 0.1 g/L, temperature = 25 ± 0.2 °C, solution pH = 7.0 ± 0.1). The white, gray, blue, red, and cyan balls denote H, C, N, O and F atoms.

cates that the most reactive sites of CIP are C5, C8, N10, O17, N19, and N24, with high Fukui indices representing electrophilic attack, *i.e.*, $f^- = 0.0417$, 0.1008, 0.0719, 0.0990, 0.0831, and 0.1472, respectively. $^{\bullet}O_2^-$ is the dominant ROS in this photocatalysis system [43]. Therefore, electrophilic attack for CIP$^{\pm}$ oxidation is focused.

Table S4 and Fig. S8 (Supporting information) present the TPs of CIP during photocatalytic degradation, and the four CIP degradation pathways are shown in Fig. 5e. Pathway I involves the photoinduced substitution of fluorine by the hydroxyl moiety for the formation of TP330 (*m/z* 330.06). The reaction occurred with the breakage of the C–F bond by attack at the C5 site ($f^- = 0.0417$). Pathway II involved defluorination and oxidation of the quinolone ring, leading to the formation of TP346 (*m/z* 346.06). TP330 and TP346 were generated *via* attack on the C5 ($f^- = 0.0417$) and C8 ($f^- = 0.1008$) sites. Pathway III involved the cleavage of the piperazine moiety *via* oxidation, which was attributed to the attack on N19 ($f^- = 0.0831$) and N24 ($f^- = 0.1472$) sites with a high Fukui index. TP362 (*m/z* 336.03) was a key intermediate in this pathway. Pathway IV involved deep defluorination after dealkylation of the piperazine moiety in Pathway III. TP344 (*m/z* 344.04) was a key intermediate formed upon the ring opening of the piperazine moiety and defluorination of CIP or TP362. Finally, mineralization of these TPs led to formation of inorganic small molecules/ions such as $CO_2$, $H_2O$, $NH_4^+$ and $F^-$ [44].

Five consecutive CIP degradation tests were performed to evaluate the reusability and stability of NbNC/g-$C_3N_4$–1 (Fig. S9 in Supporting information), and the CIP removal efficiency just slightly decreased from 97.1% to 90.1%, indicating the good reusability and high stability of NbNC/g-$C_3N_4$–1. In addition, the physicochemical properties of NbNC/g-$C_3N_4$–1 after reaction were analyzed by XRD and XPS (Fig. S10 in Supporting information), which also indicate slight changes on crystal phase and composition of the material after photocatalysis [20]. In addition, negligible Na and Nb leached during the photocatalytic reaction based on ICP-OES analysis, indicating good reusability and high stability of NbNC/g-$C_3N_4$–1.

In this study, NbNC/g-$C_3N_4$ nanohybrid was synthesized through *in-situ* transformation of $Na_2Nb_2O_6{\cdot}H_2O$ at the interface of g-$C_3N_4$, which exhibited as type-I heterojunction. The opti-

mized NbNC/g-$C_3N_4$–1 showed high photocatalytic activity for efficient photocatalytic degradation and detoxification of CIP under simulated solar light. In the NbNC/g-$C_3N_4$ nanohybrid, the electron transfer path was as follows: N 2p → O 2p → Nb 3d → C 2p. Electrons can be effectively transferred along the Nb–O–N/Nb–O–C bonds, which greatly facilitates the migration of photoexcited electrons/holes. Meanwhile, the electron density increased in g-$C_3N_4$ to form a built-in electric field, because 0.37 $e^-$ transferred from $NaNbO_3$ to g-$C_3N_4$ based on Mulliken population analysis, which can significantly boost the separation rate of charge carriers. Upon solar light irradiation, simultaneous degradation and detoxification of CIP by the NbNC/g-$C_3N_4$ nanohybrid was achieved, implying its considerable application potential in practical wastewater treatment.

## Declaration of competing interest

The authors declare that they have no known competing financial interests or personal relationships that could have appeared to influence the work reported in this paper.

## CRediT authorship contribution statement

**Hui Wang:** Writing – original draft, Validation, Resources, Methodology, Investigation, Funding acquisition, Conceptualization. **Haodong Ji:** Writing – review & editing, Validation, Supervision, Methodology, Funding acquisition, Data curation. **Dandan Zhang:** Validation, Investigation, Formal analysis, Data curation. **Xudong Yang:** Validation, Software. **Hanchun Chen:** Validation, Investigation. **Chunqian Jiang:** Writing – review & editing, Supervision, Funding acquisition, Conceptualization. **Weiliang Sun:** Validation, Methodology, Investigation, Data curation. **Jun Duan:** Validation, Methodology, Data curation. **Wen Liu:** Writing – review & editing, Validation, Supervision, Project administration, Methodology, Funding acquisition, Data curation, Conceptualization.

## Acknowledgments

Financial supports from the National Key Research and Development Program of China (Nos. 2021YFA1202500 and 2022YFF1303004), Shenzhen Science and Technology Program (No. JCYJ20220531093205013), the National Natural Science Foundation of China (NSFC) (Nos. 52100069, 52270053 and 52200084), the Beijing Natural Science Foundation (No. 8232035), the Beijing Nova Program (No. 20220484215), the Beijing National Laboratory for Molecular Sciences (No. BNLMS2023011) and Emerging Engineering Interdisciplinary-Young Scholars Project (Peking University), the Fundamental Research Funds for the Central Universities are greatly acknowledged. DFT calculations supported by the High-Performance Computing Platform of Peking University and the National Key Scientific and Technological Infrastructure project "Earth System Numerical Simulation Facility" (EarthLab) are also acknowledged. The work is also supported by the program of "Research on Advanced Treatment Technology of New Pollutants in Domestic Sewage of Residential District".

## Supplementary materials

Supplementary material associated with this article can be found, in the online version, at doi:10.1016/j.cclet.2024.110200.

## References

[1] B. Zhou, L. Chen, F. Li, et al., Chin. Chem. Lett. 34 (2023) 108558.
[2] F. Sun, X. Yang, F. Shao, et al., Chin. Chem. Lett. 34 (2023) 108563.
[3] C. Dang, F. Sun, H. Jiang, et al., J. Hazard. Mater. 400 (2020) 123225.
[4] W. Liu, Y. Li, F. Liu, et al., Water Res. 151 (2019) 8–19.
[5] J. Richard, A. Boergers, C. vom Eyser, K. Bester, J. Tuerk, Int. J. Hyg. Environ. Health. 217 (2014) 506–514.
[6] H. Ji, T. Wang, T. Huang, B. Lai, W. Liu, J. Cleaner Prod. 278 (2021) 123924.
[7] S. Li, T. Huang, P. Du, W. Liu, J. Hu, Water Res. 185 (2020) 116286.
[8] J. Xu, P. Liang, X. Shen, et al., Sep. Purif. Technol. 339 (2024) 126734.
[9] O. Baaloudj, I. Assadi, N. Nasrallah, et al., J. Water Process Eng. 42 (2021) 102089.
[10] Y. Liu, L. Chen, X. Liu, et al., Chin. Chem. Lett. 33 (2022) 1385–1389.
[11] A. Kumar, P. Raizada, A. Hosseini-Bandegharaei, et al., J. Mater. Chem. A 9 (2021) 111–153.
[12] A. Balakrishnan, E.S. Kunnel, R. Sasidharan, M. Chinthala, A. Kumar, Chem. Eng. J. 475 (2023) 146163.
[13] D. He, Z. Zhang, Y. Xing, et al., Chem. Eng. J. 384 (2020) 123258.
[14] T. Muhmood, M. Xia, W. Lei, F. Wang, Appl. Catal. B: Environ. 238 (2018) 568–575.
[15] Y.F. Xu, M.Z. Yang, B.X. Chen, et al., J. Am. Chem. Soc. 139 (2017) 5660–5663.
[16] E. Grabowska, Appl. Catal. B: Environ. 186 (2016) 97–126.
[17] X. Liu, P. Du, W. Pan, et al., Appl. Catal. B: Environ. 231 (2018) 11–22.
[18] P. Li, H. Xu, L. Liu, et al., J. Mater. Chem. A 2 (2014) 5606–5609.
[19] P. Li, S. Ouyang, Y. Zhang, T. Kako, J. Ye, J. Mater. Chem. A 1 (2013) 1185–1191.
[20] D. Zhang, J. Qi, H. Ji, et al., Chem. Eng. J. 400 (2020) 125918.
[21] M.J. Frisch, G.W. Trucks, H.B. Schlegel, et al., Gaussian 16 Rev. C.01, 2016.
[22] X. Zeng, J. Zhu, G. Zhang, et al., Chem. Eng. J. 468 (2023) 143536.
[23] S. He, E. Wu, M. Shen, ACS ES&T Eng. 3 (2023) 651–660.
[24] M.D. Segall, J.D.L. Philip, M.J. Probert, et al., J. Phy. Condens. Matter 14 (2002) 2717.
[25] S. Gao, H. Ji, P. Yang, et al., Small 19 (2023) 2206114.
[26] S. Gao, R. Wu, M. Sun, et al., Appl. Catal. B: Environ. 324 (2023) 122260.
[27] A. Yu, J. Qian, L. Liu, H. Pan, X. Zhou, Appl. Surf. Sci. 258 (2012) 3490–3496.
[28] M. Nyman, A. Tripathi, J.B. Parise, R.S. Maxwell, T.M. Nenoff, J. Am. Chem. Soc. 124 (2002) 1704–1713.
[29] Y. Yang, S. Zhao, F. Bi, et al., Appl. Catal. B: Environ. 315 (2022) 121550.
[30] A. Kumar, P. Raizada, P. Singh, R.V. Saini, A.K. Saini, Chem. Eng. J. 391 (2020) 123496.
[31] J.H. Jung, C.Y. Chen, W.W. Wu, et al., J. Phys. Chem. C 116 (2012) 22261–22265.
[32] L. Yan, T. Zhang, W. Lei, et al., Catal. Today 224 (2014) 140–146.
[33] R. Radha, Y. Ravi Kumar, M. Sakar, K. Rohith Vinod, S. Balakumar, Appl. Catal. B: Environ. 225 (2018) 386–396.
[34] H. Ji, Y. Gong, J. Duan, D. Zhao, W. Liu, Mar. Pollut. Bull. 135 (2018) 427–440.
[35] H. Ji, Y. Zhu, W. Liu, et al., Colloids Surf. A: Physicochem. Eng. Asp. 561 (2019) 373–380.
[36] X. Yang, F. Li, W. Liu, et al., Appl. Catal. B: Environ. 324 (2023) 122202.
[37] J. Qi, X. Yang, P.Y. Pan, et al., Environ. Sci. Technol. 56 (2022) 5200–5212.
[38] H. Shi, G. Chen, C. Zhang, Z. Zou, ACS Catal. 4 (2014) 3637–3643.
[39] X. Yang, J. Duan, J. Qi, et al., J. Hazard. Mater. 445 (2023) 130576.
[40] H. Zhang, Y. Wang, S. Zuo, et al., J. Am. Chem. Soc. 143 (2021) 2173–2177.
[41] J. Low, J. Yu, M. Jaroniec, S. Wageh, A.A. Al-Ghamdi, Adv. Mater. 29 (2017) 1601694.
[42] J. Duan, L. Chen, H. Ji, et al., Chin. Chem. Lett. 33 (2022) 3172–3176.
[43] F. De Vleeschouwer, V. Van Speybroeck, M. Waroquier, P. Geerlings, F. De Proft, Org. Lett. 9 (2007) 2721–2724.
[44] Y. Wang, X. Sun, J. Ma, et al., Sep. Purif. Technol. 337 (2024) 126392.